How Ligands Affect Resistive Switching in Solution-Processed HfO_2 Nanoparticle Assemblies

Jiaying Wang[1], *Satyan Choudhary*[2], *Jonathan De Roo*[3], *Katrien De Keukeleere*[3], *Isabel Van Driessche,*[3] *Alfred J. Crosby*[2], and *Stephen S. Nonnenmann*[1,*]

1. J. Wang, Prof. S.S. Nonnenmann

Department of Mechanical and Industrial Engineering, University of Massachusetts-Amherst, 160 Governors Drive, 219 Engineering Laboratory I, Amherst, MA, 01003, USA, *e-mail: ssn@umass.edu

2. S. Choudhary, Prof. A.J. Crosby

Polymer Science and Engineering Department, University of Massachusetts Amherst, Silvio O. Conte National Center for Polymer Research, 120 Governors Drive, Amherst, MA 01003, USA

3. Jonathan De Roo, Katrien De Keukeleere, Isabel Van Driessche

Department of Chemistry, Ghent University, Krijgslaan 281- building S3, B-9000 Gent, Belgium

Abstract

Rapid growth of resistive random access memory (ReRAM) requires fully understanding the various complex, defect-mediated underlying mechanisms to further improve performance. While thin film oxide materials have been extensively explored, the switching properties of nanoparticle assemblies remain underexplored, due to difficulties in

fabricating ordered structures. Here a simple flow coating method for facile deposition of highly ordered HfO_2 nanoparticle nanoribbon assemblies is employed. We observe the resistive switching character of nanoribbons comprising HfO_2 nanoparticles as a function of ligand length, using oleic, dodecanoic, and undecenoic acid capping layers. Through direct comparisons of the forming process, operating set/reset voltages, and resistance states, we demonstrate tunability in the resistive switching response as adjusted by varying the ligand types, thus providing a base correlation for solution-processed ReRAM device fabrication.

Introduction

Due to the scaling limits of flash memory, recent studies have focused on emerging non-volatile devices such as resistive random access memory (ReRAM),[1-3] phase change memory (PCM)[4] and ferroelectric random access memory (FeRAM)[5]. Of these, ReRAM exhibits outstanding properties such as fast switching speed, good reliability and low power consumption, thus the promise for the next generation nonvolatile memory device.[1-2] Resistive switching behavior describes a reversible change between a high resistance state (HRS) and low resistance state (LRS) within a metal-oxide-metal structure that depends on the history of an applied electric field.[6] Generally, an electroforming process creates ionic defects within the oxide layer of the pristine device under a high applied bias, thus initiating the subsequent SET/RESET operations. Despite intense research focus on the fabrication and characterization of resistive switching oxide thin films,[7-10] nanoparticles,[11] and nanowires,[12] the development of rapid and low-cost solution-processed systems as an alternative to complicated multistep lithographic approaches remains stunted. Hafnia, HfO_2, is a prototype resistive switching binary oxide that exhibits excellent scalability, reliability, and CMOS compatibility in both amorphous and crystalline structure.[13] Here we introduce a facile, low-cost method to prepare HfO_2 nanocrystals in highly ordered nanoribbon arrays via convective self-assembly. Recent studies demonstrated the charge transport effect

within solution-processed semiconductors such as colloidal CdSe quantum dots[14] and PbS photovoltaic nanoparticles,[15] but not for resistive switching nanoparticles where the capping ligand interparticle interface can profoundly affect the response.[16-17] Correlating the changes in ligand chemistry with operating voltages, device stability, and switching mechanism are therefore critical to modulating and improving the performance of solution-processed systems.

This study systematically compares the resistive switching behavior of individual nanoribbons comprising single-crystalline HfO_2 nanocrystals (NCs) capped with oleic, dodecanoic, and undecanoic acid ligands of various lengths. The convective self-assembly approach addresses typical issues facing nanocrystal assembly (i.e. scalability and periodicity) to produce ordered nanostructure arrays without the complexity of fabrication templates or lithographic patterning.[18] We previously demonstrated memristive functionality within nanoribbons comprising perovskite strontium titanate ($SrTiO_3$) nanocubes that retained or changed its memristive functionality as transferred from the original substrate to a second, arbitrary substrate.[19] In this study HfO_2 nanoribbons exhibit both threshold switching (TS) and bipolar resistive switching (BRS) induced by controlling the conductive filament morphology, similar to recent studies of HfO_2 thin films.[20] We determined that both the forming voltage and SET voltage scale with ligand length, suggesting that the interparticle tunnel distance is responsible for the carrier transport within HfO_2 ribbon.

Results and discussion

HfO_2 nanocrystals are synthesized from hafnium chloride and benzyl alcohol in a solvothermal process according to De Roo et al.[21-22] After synthesis, the nanocrystals as washed with diethyl ether and functionalized with a carboxylic acid (oleic acid, dodecanoic acid, or undecenoic acid). Deposition of the HfO_2 NCs into nanoribbon assemblies required the implementation of the ‘stop-and-go’ flow coating method previously demonstrated for other colloidal systems.[1–3] Details are introduced in the method section. Nanoribbons were fabricated

comprising HfO_2 NCs capped with three types of ligands; oleic acid, dodecanoic acid, and undecenoic acid, labeled hereafter as HfO_2-O, HfO_2-D and HfO_2-U, respectively. Figure 1 shows the nanocrystalline morphology of the HfO_2 nanoparticles and schematic illustration of the convective self-assembly processes. The transmission electron microscopy (TEM) image of HfO_2-D in Figure 1a shows the as-prepared nanocrystal morphology, while the inset shows a high-resolution TEM image that indicates NP dimensions on the order of 5 nm. The x-ray diffraction (XRD) in Figure 1b reveals the phase pure, monoclinic structure of HfO_2 NPs. The stop-and-go flow coating method, as illustrated in Figure 1c, deposits nanoparticles onto a hard substrate by flowing a colloidal solution under the flexible coating blade. The height and the width of the ribbon can be precisely controlled from nanoscale to bulk dimensions by varying the stop time of the state shift, thus enabling the direct fabrication of nanostructures ranging from individual nanoribbons to nanocrystal films. The optical microscopy image in Figure 1d shows highly ordered arrays of individual HfO_2 nanoribbons prepared by flexible blade deposition with an average width of 6 μm. Figure 1e shows the three-dimensional topographic profile of an individual HfO_2 nanoribbon collected via atomic force microscopy (AFM), indicating that nanoribbons possess a wedge-like cross sectional profile.

Conductive AFM (c-AFM) is a powerful tool for studying RS behavior with the ability to spatially resolve local heterogeneities within the electronic response, and probe the current distribution simultaneously.[11, 23-24] Figure 2a illustrates the general c-AFM setup, where a Pt/Ir coated silicon tip is placed in direct contact with the surface of individual HfO_2 nanoribbons, creating a Pt/Ir/HfO_2 NCs/Pt test structure. Here the bias is applied to the bottom Pt electrode, with the current flowing through the ribbon vertically, which is then read via a grounded, conductive tip rastering along the top surface of the nanoribbon.

No current is measured across the nanoribbons before a forming process is induced under a large voltage of 10 V applied to the ribbon locally. The large applied field manifests as a bright

spot corresponding to a highly conductive region, as shown in Figure 2b on the HfO_2-D system. Current imaging was conducted by scanning a single nanoribbon with an applied voltage of +2.5 V (Figure 2b), followed by a scan under -2 V applied bias (Figure 2c), suggesting the conducting path formed during forming/SET process.

The electroforming process induced filament formation within HfO_2 nanoribbons capped with the three ligand systems is shown in Figure 3a, where the HfO_2-U, HfO_2-D and HfO_2-O systems displayed forming voltages of 6.1 V, 8.2 V and 10 V, respectively. Note that HfO_2-O requires an applied voltage larger than 10 V, which is the limit of the external bias source of the instrument. Figure 3b shows the semi-log I-V response of the three ligand capped HfO_2 nanoribbons. They all display typical bipolar switching character, where the SET and RESET process occur under positive and negative voltage, respectively, and exhibit a clear variation in operating voltage, current level and the resistance ratio between them. Here we found the HfO_2-D displays a smaller set voltage of 1.2 V while HfO_2-O requires a larger set voltage of 2 V. A standard 1 MΩ resistor was used to transition between operative bipolar resistive switching and threshold switching modes in the nanoribbons. The current-voltage (I-V) character observed in Figure 3c represents the threshold behavior under voltage sweeping (±2 V, 1 Hz) when the resistor is connected in series with the HfO_2-U system. Unlike the bipolar switching the threshold switching shows a symmetric I-V curve. Moreover, it shows a high resistance (10^9 Ω) initially followed by an abrupt increase in current level upon reaching a threshold voltage of approximately +1 V. The ribbon maintains LRS and recovers to the HRS suddenly at a hold voltage of +0.25 V. This threshold behavior can be tuned with the external resistor for each sample, exhibiting similar operating voltage ranges and stability. Figure 3d shows 50 switching cycles within a single HfO_2-U nanoribbon, suggesting the TS behavior remains stable, with a selectivity of 10^3. When the resistor is removed, the typical bipolar resistive switching hysteresis is observed.

To evaluate the effect of ligand length on memristive behavior we estimated the interparticle spacing of the three samples based on the covalent chain length: HfO_2-U (1.44 nm), HfO_2-D (1.57 nm), HfO_2-O (2.2 nm). Figure 4a plots the SET and RESET voltage distribution for bipolar switching as a function of the ligand length. The SET voltage clearly scales with increasing ligand length, while the RESET voltage exhibits a smaller dependence on length. An increase in the V_{SET} distribution can also be observed in the statistical plot with the increased ligand length, while for V_{RESET}, however, no clear correlation is found. Figure 4b presents the cumulative distribution function of the LRS and HRS of the three ligand types. The results were collected using DC sweeping mode at a read voltage of 0.5 V. The resistance in LRS exhibits a much smaller variation compared to the large variations observed for HRS for all three types. The HfO_2-O system shows a large HRS fluctuation range of about 10^4 while the HfO_2-U and HfO_2-D systems show improved uniformity of about 10^3 and 10^2, respectively. Furthermore, HfO_2-U possesses a higher HRS resistance that results in a smaller leakage current, which is attributed to its shorter ligand length. In general, the variation of LRS and V_{RESET} come from either varying filament diameter size or the number of conducting filaments formed during the SET process, while the variation in HRS and V_{SET} is highly dependent on variations in the tunneling gap.[13]

Previous studies of PbSe NCs showed that the carrier mobility depends on nanoparticle size and the ligand length, the latter of which determines the interparticle tunnel distance.[16] Using the same nanoparticle size for all samples, we posit the variation in the ligand length causes the observed difference in RS behavior. The charge transport mechanism involves sequential electron hopping through nanoparticles, as described by an Arrhenius-type activated tunneling model:[17]

$$\sigma(\delta, T) = \sigma_0(e^{-\beta\delta})e^{-E_A/k_BT}, \quad (1)$$

where β is the electron-tunneling coefficient that is determined by the chemical nature of the ligand, δ is the average interparticle spacing depends on the length of the ligand and E_A is the activation energy. Here E_A is determined by the equation:

$$E_A = \frac{e^2}{8\pi\varepsilon\varepsilon_0}\left(\frac{1}{r} - \frac{1}{r+\delta}\right), \quad (2)$$

where *r* is the average radius of the particles, δ is the interparticle distance, and ε is the dielectric constant of the matrix by the ligand. Here both the forming (Figure 3a) and the subsequent SET process (Figure 4a) display a ligand length dependence, as both V_F and V_{SET} increase with increasing ligand length.

During the charge transfer process the ligand facilitates electron tunneling by effectively serving as an insulating spacer.[25] Using the c-AFM tip as the top electrode forms a Pt/Ir tip-HfO_2 NCs-bridge-metal structure, where the term bridge indicates the capping ligand separating neighboring NCs and the metal bottom electrode with the bulk HfO_2 NCs. When a positive voltage is applied to the bottom electrode during the electroforming process, the high electric field enables the creation of oxygen vacancies within the NCs and induces migration toward the tip along the grain boundary to form a low resistance conductive path.[26] The electrons injected from the tip under the negative voltage thus pass through the conductive channel and tunnel between NPs, inducing a transition from HRS to LRS. When a negative voltage is applied to the bottom electrode, the oxygen vacancies migrate towards the counter electrode as driven by the electric field of opposite sign, thus severing the conductive channel. The observed TS and BRS characteristics are explained by variations in the morphology of the conducting filament. Limiting the current flow with an external resistor induces an instability within the filament, ultimately resulting in filament rupture after the applied voltage is removed. Once the conducting filament formed, any subsequent growth is suppressed due to the small amount of current passing through, resulting

in a fragile filament. Conversely, the current increases when the resistor is removed such that a stronger, more continuous filament is formed, manifesting as bipolar resistive switching.

To demonstrate a solution-processed memristive platform, we fabricated a crossbar device with a flow-coated HfO_2-U thin film sandwiched between Ti top and Pt bottom electrode. The schematic of the cross-point HfO_2-U test structure is shown in Figure 5a. Using the same solution concentration, the width of the ribbon is simply extended by varying the stopping distance and substrate velocity. Using the longer stopping distance, we fabricated a 5x5 μm^2 crossbar type device comprising a 40 nm thick HfO2-U thin film sandwiched between 30 nm thick Pt electrodes. The bipolar resistive switching I-V response was measured by sweeping a DC voltage from -0.5 V to +1.5 V after a forming process using a compliance current of 100 µA (Figure 5b). An ALD-deposited 10 nm HfO_2 ReRAM device with the same area was fabricated for comparison. Here the solution-processed HfO_2-U device clearly exhibits smaller operating voltages, narrow distribution/increased uniformity, and larger ON/OFF ratio as shown in Figure 5c, d. The average SET and RESET voltages were 0.97 V and -0.36 V, respectively for HfO_2-U; the ALD-deposited HfO_2 displayed values of 3.2 V and -2.5 V, respectively. The ON/OFF ratio improved from 10 for ALD HfO_2 to 10^5 for the HfO2-U at the expense of a small decrease in the uniformity of the resistance. Thus, the solution-processed device exhibits both stable switching behavior and small operating voltages that are competitive with more commonly employed ALD-deposited HfO_2 ReRAM devices.

Conclusion

In summary, we introduced a facile, inexpensive and versatile fabrication method to produces memristive nanoribbon structures comprising solution-processed, binary hafnium oxide nanoparticles. We demonstrated that ligand length direct affects the resistive switching behavior by comparing three commonly employed ligand chemistries. Our c-AFM results showed that individual HfO_2 nanoribbons demonstrated both threshold switching and bipolar resistive

switching modes, dependent upon an external resistance applied to the system, which attributed to changes in the filament morphology. The forming and SET voltage scale strongly with increasing ligand length, while the reset voltage displays only a slight dependence. Moreover, different ligands affect the stability of the resistance in HRS due to the variation in the tunneling distances. We conclude that intrinsic oxygen vacancies formed during hydrothermal process are responsible for the switching behavior, and the operating parameters correlate directly with ligand length. Finally, our solution-based device demonstrated promising advantages, including low cost and time saving process, lower operating voltages, increased uniformity, and larger ON/OFF ratio compares to the typical ALD thin film HfO_2 memory device. The chosen ligands for this study are frequently used for nanoparticle stabilization, and thus should immediately apply to optimizing resistive switching behavior in other complex oxide nanoparticle systems.

Methods. HfO_2 nanocrystals (0.4 mmol HfO_2) were synthesized from $HfCl_4$ and benzyl alcohol according to De Roo et al.[cite] After solvothermal synthesis and washing with diethyl ether, the nanocrystals are redispersed in chloroform (4mL). 0.2 mmol of fatty acid (oleic acid, dodecanoic acid, or 10-undecenoic acid) was added to the milky suspension. In case of 10-undecenoic acid, 5 % of dodecanoic was also added to ensure colloidal stability. Under stirring or ultrasonication, oleylamine (0.15 mmol or 50 µL) was added until a transparent and colorless suspension was obtained. Finally, the particles are purified three times by adding acetone to induced precipitation, followed by centrifugation and resuspension in chloroform. After the last purification, the nanocrystals were dispersed in toluene.

HfO_2 Nanoribbon Convective Self-Assembly: The custom-built flow coating instrument uses a silicon wafer (University Wafer Inc.) cut to an edge length of 15 mm as a fixed blade. This blade is attached to a tilt-translation stage with pitch, roll and height control capability. With visual guidance, the blade edge is aligned parallel to the substrate at the approximate height 150-300 µm for all coating procedure. The substrate is attached to a programmable nanopositioner

(Burleigh Inchworm controller 8200), which performs a series of stop-and-go steps. Here the primary variables that control the nanoribbon geometry (height, width) are solution concentration, stop time (t_d), spacing (d) and velocity (v). The HfO_2 nanoribbons in this study were prepared using the following parameters: v = 1500 µm/s, solution concentration = 1 mg/ml, d = 200 µm, and a t_d between 1000 to 6000 ms. Different stop times were used to vary the nanoribbon height (h) and width (w), t_d = 1000 ms (h = 80 nm, w = 8 µm), t_d = 3000 ms (h = 160 nm, w = 13 µm), and t_d = 6000 ms (h = 230 nm, w = 17 µm). A fixed volume of HfO_2 NC solution (10 µl) is injected between the fixed blade and the substrate, where capillary forces confine the solution to the blade edge. The HfO_2 NC nanoribbons were deposited directly on silicon wafer substrates (undoped <100>, University Wafer Inc.). Before deposition all substrates and blades were rinsed with isopropyl alcohol and toluene then dried after each step with a filtered stream of N_2 gas.

Acknowledgements

This research was partially supported by University of Massachusetts-Amherst start-up funding and the UMass Center for Hierarchical Manufacturing (CHM), a NSF Nanoscale Science and Engineering Center (CMMI-1025020). A.J.C and S.C. gratefully acknowledge financial support from the Army Research Office (W911NF-14-1-0185). The authors also acknowledge use of the facilities at the CHM Conte Nanotechnology Cleanroom for thin film deposition and plasma clean processes. J.D.R. thanks Fulbright and B.A.E.F. for funding. J.W. performed all substrate/electrode preparation, c-AFM measurements, transport analysis, and wrote the manuscript. S.C. performed all nanoribbon fabrication and transfer to arbitrary substrates. J.D.R and K.D.K performed hydrothermal synthesis and structural characterization of HfO_2 NCs. A.J.C. co-wrote the manuscript and supervised all nanoribbon formation. S.S.N. lead the overall project, supervised general fabrication, local probe, and data analysis studies and wrote the manuscript.

Figures and Figure Captions

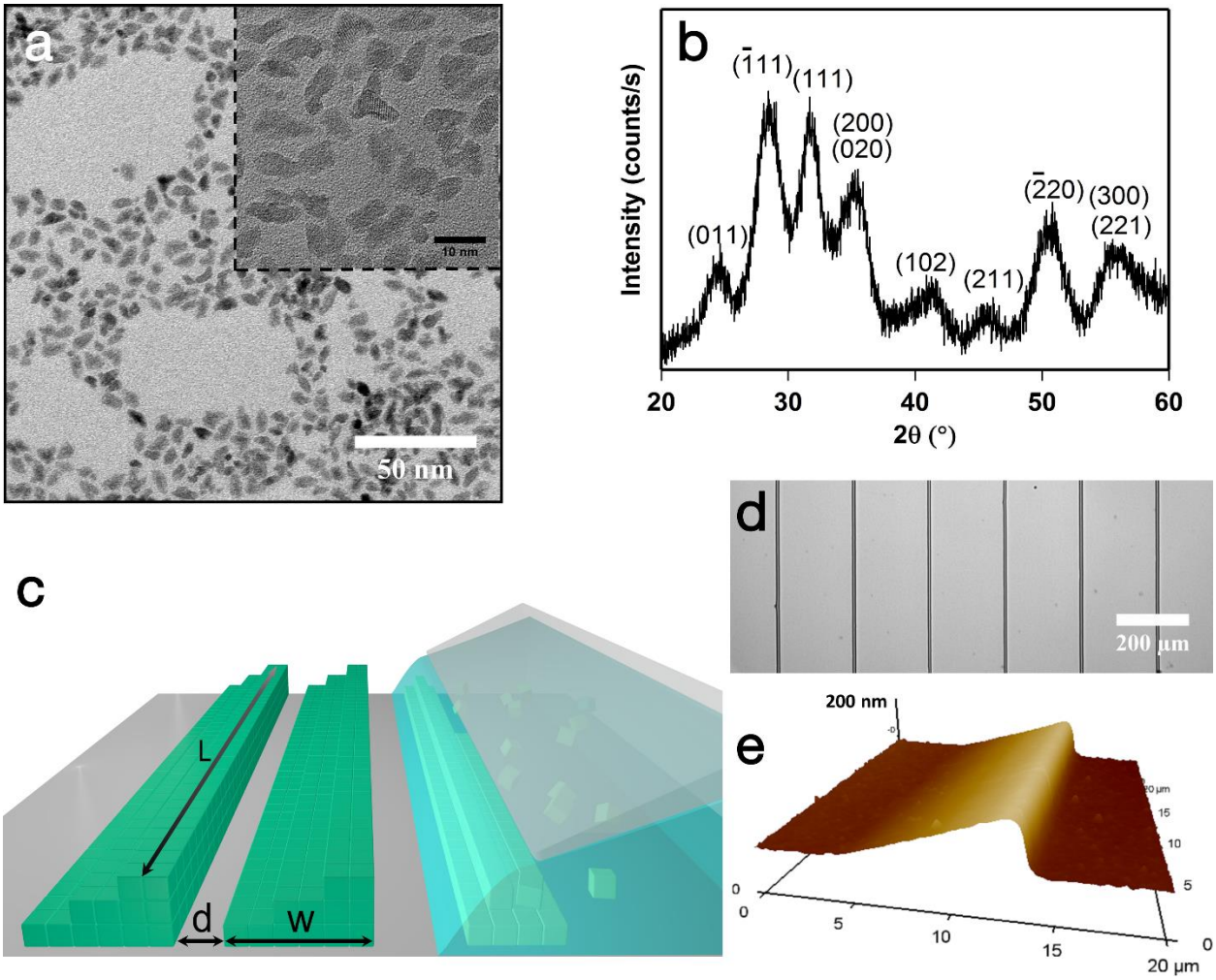

Figure 1 a, TEM image shows the crystalline structure of HfO_2 nanoparticles with the scale bar denotes 50 nm. Inset: HRTEM image of NCs indicates the lattice fringe and size of 5 nm. **b**, X-ray diffraction patterns of monoclinic HfO_2. **c**, An illustration of the "stop-and-go" flow coating process. The shape and profile of the ribbon are confirmed by **d**, three-dimensional AFM image.

e, An optical micrograph (scale bar 200 µm) showing highly ordered ribbons comprising HfO_2 nanoparticles.

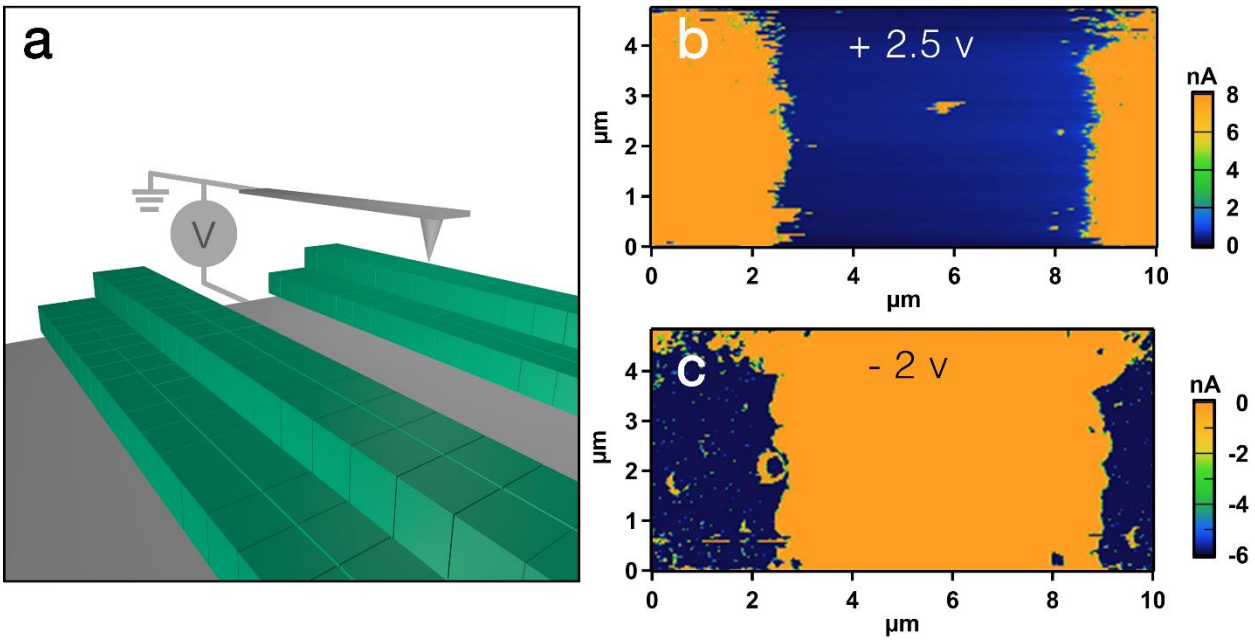

Figure 2 a, An illustration of the c-AFM measurement setup across an individual HfO_2 nanoribbon. **b**, Current mapping of individual HfO_2-D ribbon with an applied voltage of +2.5 V, displaying a yellow conducting spot formed after a forming voltage of +6 V. **c**, Corresponding current mapping of the area with an applied voltage of -2 V. No observed conducting spot indicates the locally reset process occurred.

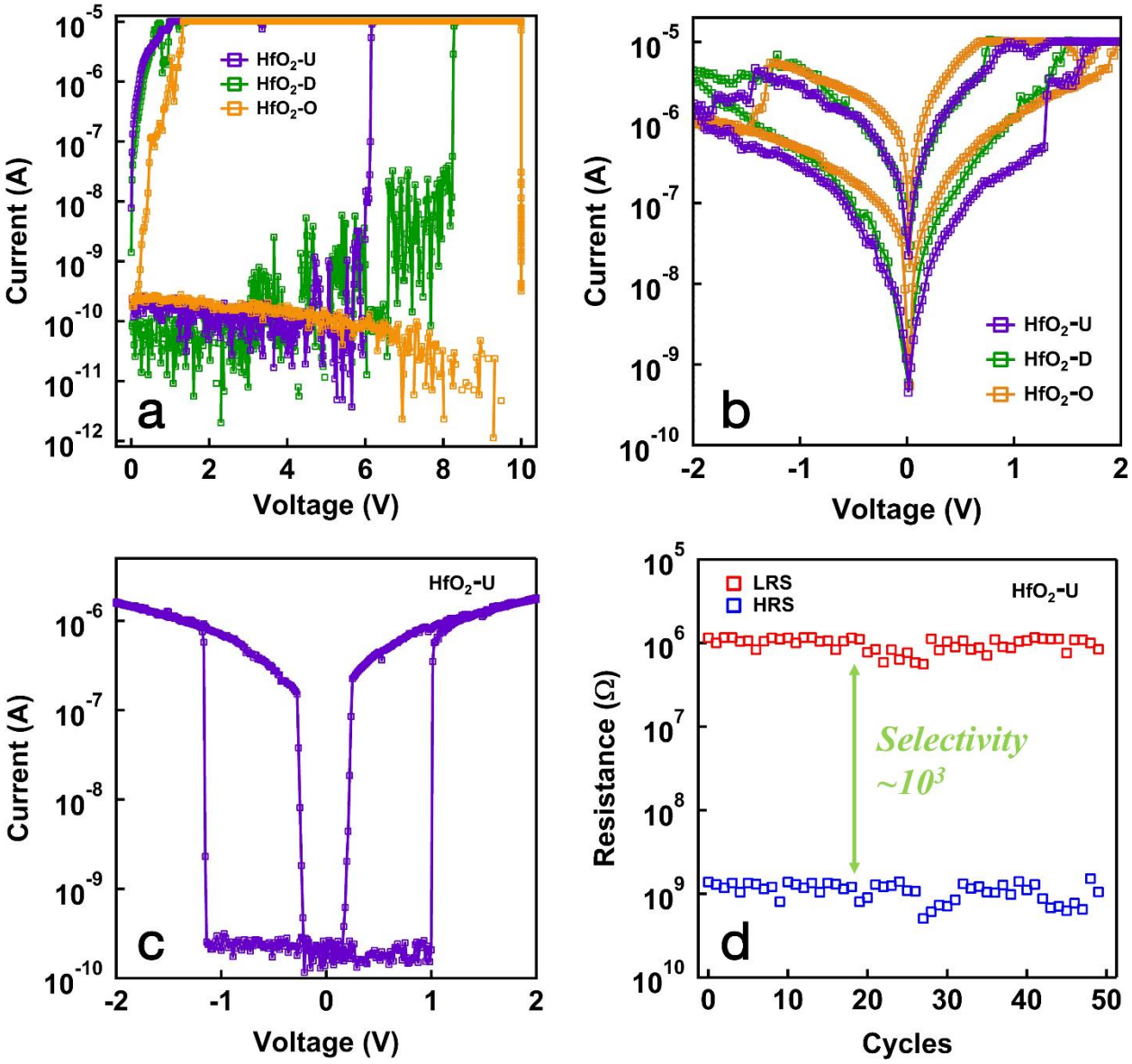

Figure 3 a, I-V curves for the forming process of HfO_2-U, HfO_2-D and HfO_2-O, respectively. **b**, Representative I-V response of BRS for three samples. **c**, I-V curve of the TS behavior of HfO_2-U sample. **d**, 50 cycles endurance of TS by sweeping at a read voltage of 0.5 V, showing a selectivity of 10^3.

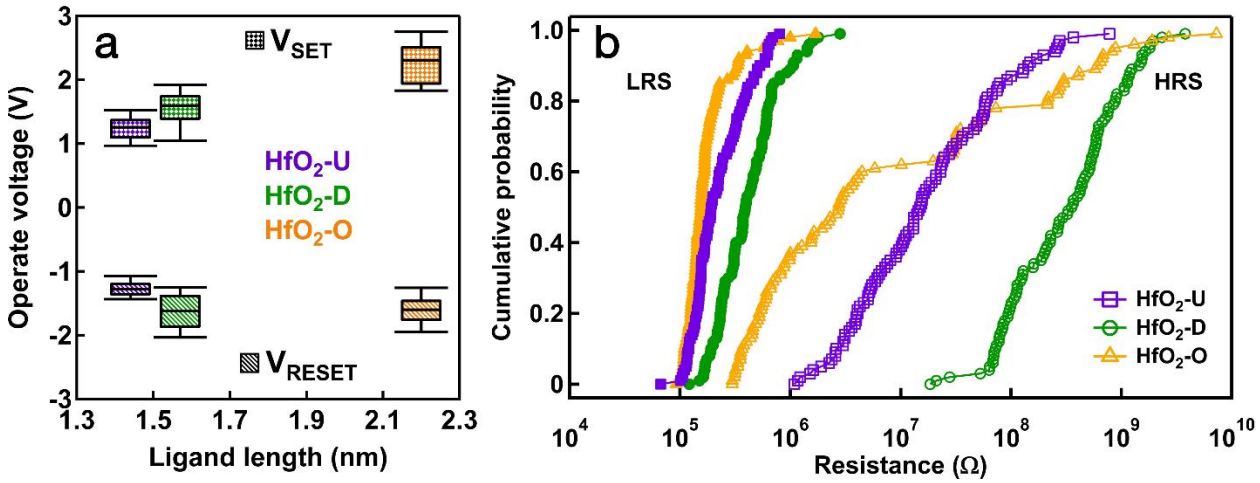

Figure 4 a, The statistical distribution plot of switching voltages as a function of ligand length. Both V_{SET} and its distribution scale with increasing ligand length. **b**, The cumulative probability for the LRS and HRS of HfO_2-U (purple; square), HfO_2-D (green; circle), and HfO_2-O (orange; triangle), respectively.

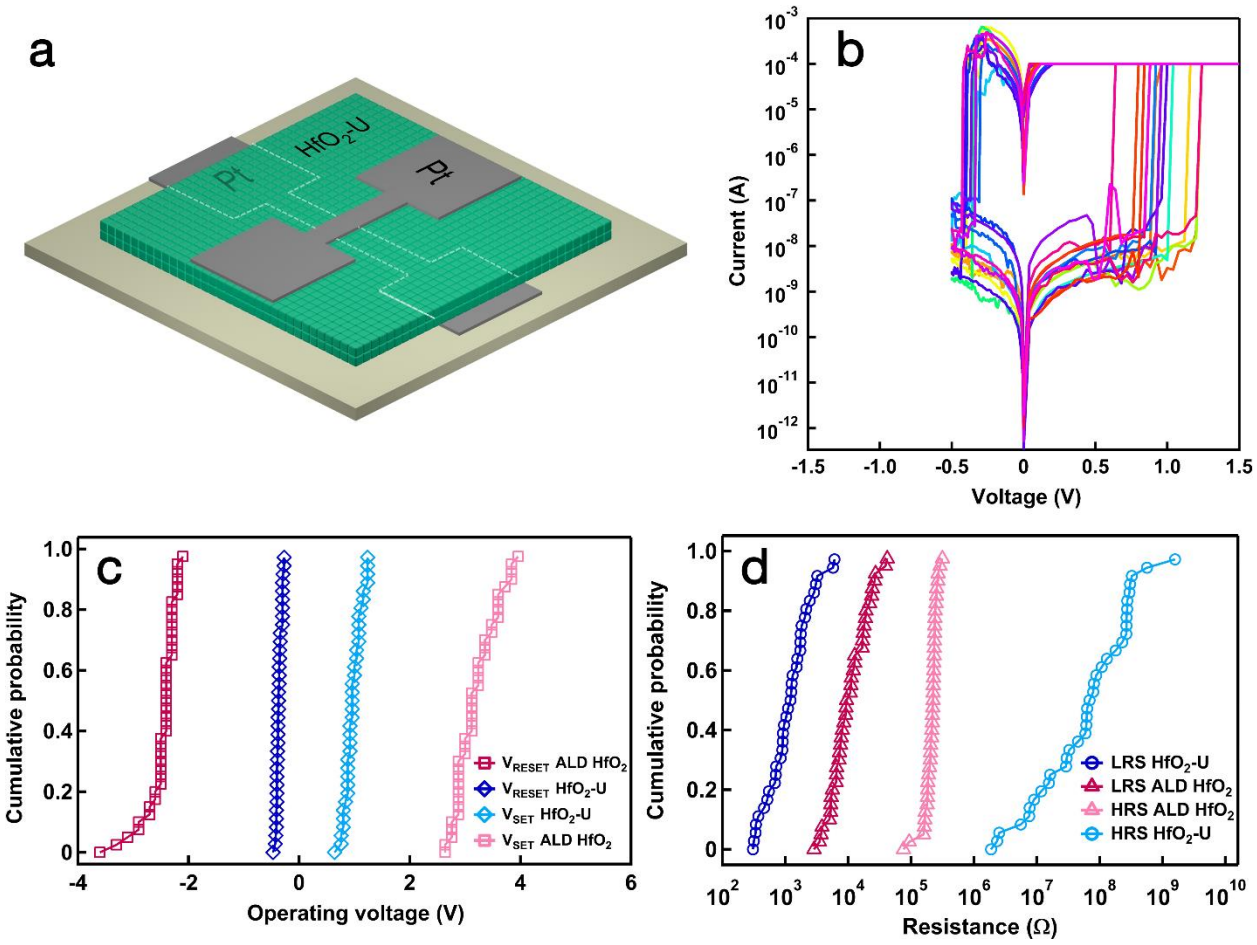

Figure 5 a, Schematic of a single Pt/HfO2-U/Pt ReRAM device. **b**, The representative I-V characteristics of Pt/HfO2-U/Pt ReRAM device. **c**, Comparative statistic cumulative probability of the operating voltage for HfO_2-U and ALD-prepared HfO_2. **d**, The cumulative probability of the resistances in each state of HfO_2-U and ALD-prepared HfO_2.

References

1. Waser, R.; Aono, M., Nanoionics-based resistive switching memories. *Nat Mater* **2007,** *6* (11), 833-40.
2. Sawa, A., Resistive switching in transition metal oxides. *Materials Today* **2008,** *11* (6), 28-36.
3. Ilia, V.; Rainer, W.; John, R. J.; Michael, N. K., Electrochemical metallization memories—fundamentals, applications, prospects. *Nanotechnology* **2011,** *22* (25), 254003.
4. Ielmini, D.; Lacaita, A. L., Phase change materials in non-volatile storage. *Materials Today* **2011,** *14* (12), 600-607.

5. Nonnenmann, S. S.; Gallo, E. M.; Spanier, J. E., Redox-based resistive switching in ferroelectric perovskite nanotubes. *Applied Physics Letters* **2010,** *97* (10), 102904.
6. Yang, J. J.; Pickett, M. D.; Li, X.; OhlbergDouglas, A. A.; Stewart, D. R.; Williams, R. S., Memristive switching mechanism for metal//oxide//metal nanodevices. *Nat Nano* **2008,** *3* (7), 429-433.
7. Waser, R.; Dittmann, R.; Staikov, G.; Szot, K., Redox-Based Resistive Switching Memories – Nanoionic Mechanisms, Prospects, and Challenges. *Advanced Materials* **2009,** *21* (25-26), 2632-2663.
8. Valov, I., Redox-Based Resistive Switching Memories (ReRAMs): Electrochemical Systems at the Atomic Scale. *ChemElectroChem* **2014,** *1* (1), 26-36.
9. Chang, T.-C.; Chang, K.-C.; Tsai, T.-M.; Chu, T.-J.; Sze, S. M., Resistance random access memory. *Materials Today* **2016,** *19* (5), 254-264.
10. Kyung Min, K.; Doo Seok, J.; Cheol Seong, H., Nanofilamentary resistive switching in binary oxide system; a review on the present status and outlook. *Nanotechnology* **2011,** *22* (25), 254002.
11. Schmidt, D. O.; Hoffmann-Eifert, S.; Zhang, H.; La Torre, C.; Besmehn, A.; Noyong, M.; Waser, R.; Simon, U., Resistive Switching of Individual, Chemically Synthesized TiO2 Nanoparticles. *Small* **2015,** *11* (48), 6444-6456.
12. Nagashima, K.; Yanagida, T.; Oka, K.; Taniguchi, M.; Kawai, T.; Kim, J.-S.; Park, B. H., Resistive Switching Multistate Nonvolatile Memory Effects in a Single Cobalt Oxide Nanowire. *Nano Letters* **2010,** *10* (4), 1359-1363.
13. Wong, H. S. P.; Lee, H. Y.; Yu, S.; Chen, Y. S.; Wu, Y.; Chen, P. S.; Lee, B.; Chen, F. T.; Tsai, M. J., Metal–Oxide RRAM. *Proceedings of the IEEE* **2012,** *100* (6), 1951-1970.
14. Voznyy, O.; Sutherland, B. R.; Ip, A. H.; Zhitomirsky, D.; Sargent, E. H., Engineering charge transport by heterostructuring solution-processed semiconductors. **2017,** *2*, 17026.
15. Niu, G.; Wang, L.; Gao, R.; Ma, B.; Dong, H.; Qiu, Y., Inorganic iodide ligands in ex situ PbS quantum dot sensitized solar cells with I-/I3- electrolytes. *Journal of Materials Chemistry* **2012,** *22* (33), 16914-16919.
16. Liu, Y.; Gibbs, M.; Puthussery, J.; Gaik, S.; Ihly, R.; Hillhouse, H. W.; Law, M., Dependence of Carrier Mobility on Nanocrystal Size and Ligand Length in PbSe Nanocrystal Solids. *Nano Letters* **2010,** *10* (5), 1960-1969.
17. Yu, X.; Malvankar, N.; Landis, R.; Eymur, S.; Miranda, O. R.; Rotello, V. M., Impedance Spectroscopy of Ionic Ligand-Modulated Charge Transport of Gold Nanoparticle Films. *Small* **2015,** *11* (31), 3814-3821.
18. Kim, H. S.; Lee, C. H.; Sudeep, P. K.; Emrick, T.; Crosby, A. J., Nanoparticle Stripes, Grids, and Ribbons Produced by Flow Coating. *Advanced Materials* **2010,** *22* (41), 4600-4604.
19. Wang, J.; Choudhary, S.; Harrigan, W. L.; Crosby, A. J.; Kittilstved, K. R.; Nonnenmann, S. S., Transferable Memristive Nanoribbons Comprising Solution-Processed Strontium Titanate Nanocubes. *ACS Applied Materials & Interfaces* **2017,** *9* (12), 10847-10854.
20. Sharath, S. U.; Vogel, S.; Molina-Luna, L.; Hildebrandt, E.; Wenger, C.; Kurian, J.; Duerrschnabel, M.; Niermann, T.; Niu, G.; Calka, P.; Lehmann, M.; Kleebe, H.-J.; Schroeder, T.; Alff, L., Control of Switching Modes and Conductance Quantization in Oxygen Engineered HfOx based Memristive Devices. *Advanced Functional Materials* **2017,** *27* (32), 1700432-n/a.
21. De Roo, J.; Van den Broeck, F.; De Keukeleere, K.; Martins, J. C.; Van Driessche, I.; Hens, Z., Unravelling the Surface Chemistry of Metal Oxide Nanocrystals, the Role of Acids and Bases. *Journal of the American Chemical Society* **2014,** *136* (27), 9650-9657.
22. De Roo, J.; Van Driessche, I.; Martins, J. C.; Hens, Z., Colloidal metal oxide nanocrystal catalysis by sustained chemically driven ligand displacement. *Nat Mater* **2016,** *15* (5), 517-521.
23. Lee, M. H.; Hwang, C. S., Resistive switching memory: observations with scanning probe microscopy. *Nanoscale* **2011,** *3* (2), 490-502.

24. Lee, H.; Kim, H.; Van, T. N.; Kim, D.-W.; Park, J. Y., Nanoscale Resistive Switching Schottky Contacts on Self-Assembled Pt Nanodots on SrTiO3. *ACS Applied Materials & Interfaces* **2013,** *5* (22), 11668-11672.
25. Adams, D. M.; Brus, L.; Chidsey, C. E. D.; Creager, S.; Creutz, C.; Kagan, C. R.; Kamat, P. V.; Lieberman, M.; Lindsay, S.; Marcus, R. A.; Metzger, R. M.; Michel-Beyerle, M. E.; Miller, J. R.; Newton, M. D.; Rolison, D. R.; Sankey, O.; Schanze, K. S.; Yardley, J.; Zhu, X., Charge Transfer on the Nanoscale: Current Status. *The Journal of Physical Chemistry B* **2003,** *107* (28), 6668-6697.
26. Lanza, M.; Bersuker, G.; Porti, M.; Miranda, E.; Nafría, M.; Aymerich, X., Resistive switching in hafnium dioxide layers: Local phenomenon at grain boundaries. *Applied Physics Letters* **2012,** *101* (19), 193502.